A Comparative Electrochemical Study of 2H/1T Phases of MoS_2 and Designing 1T-MoS_2@Cu_2S for High-Performance Supercapacitor

Arkapriya Das[a], Alakananda Paul[a], Ankita Mondal[a], Kaushik Pal[b,c], Bhanu Bhusan Khatua[a]*

[a] *Materials Science Centre, Indian Institute of Technology Kharagpur, Kharagpur-721302*

[b] *Centre for Nanotechnology, Indian Institute of Technology Roorkee, Roorkee, 247667*

[c] *Department of Mechanical and Industrial Engineering, Indian Institute of Technology Roorkee, Roorkee, 247667*

*corresponding author

Email id: khatuabb@matsc.iitkgp.ac.in

Contact: (+91) 3222 283982 (off)

Materials characterization

The X-ray diffraction (XRD) pattern of the prepared composite was recorded by an X'Pert PRO diffractometer (PANalytical, Netherlands) with nickel-filtered Cu Kα (λ = 0.15404 nm) at a scanning rate of 0.25° min^{-1}. FTIR spectroscopic analysis was done using NEXUS 870 FTIR (Thermo Nicolet) to study the characteristic vibration mode of the prepared materials. The morphology of the prepared materials and mapping analysis were investigated using a field emission scanning electron microscope (FE-SEM, MERLIN and Carl Zeiss-SUPRATM 40) and the energy-dispersive X-ray spectroscopy (EDS, Oxford EDS detector). The bulk morphology, SAED pattern, high resolution transmission electron microscope (HRTEM) and elemental mapping of the synthesized material were acquired using a high resolution transmission electron microscope (JEOL, JEM- ARM 300 F2). Raman spectra were recorded from a Raman triple spectrometer (T-64000, HORIBA Jobin Yvon) associated with a synapse detector. X–ray photoelectron spectroscopic (XPS) analysis was done using a PHI 5000 Versa Probe II X–ray photoelectron spectrometer [Al Kα source ~1486 eV]. The specific surface area and pore size distribution of the prepared materials were estimated using BET (Brunauer-Emmett-Teller) analyser (model: AUTOSORB-1, Quantachrome Instruments, USA). The band gap energy was calculated from the UV-visible spectrum using Agilent Cary 5000 UV-Vis-NIR Spectrophotometer (range~175–3300 nm). The contact angle measurement was carried out using Surface electro optics Phoenix 300 Touch (0~180°±0.1 accuracy). The concentration of Mo, Cu and S in the composite was evaluated with inductively coupled plasma atomic emission spectroscopy (ICP-AES) (Perkin Elmer 7000D).

Morphological analysis

The observed dendritic structure of hy 1T-MoS_2@Cu_2S composite arises from a kinetically controlled growth mechanism, specifically driven by diffusion-limited aggregation (DLA)

during hydrothermal synthesis. Under the optimized condition (80 °C), Cu^{2+} ions complex with EDA to form $[Cu(En)_2]^{2+}$, which moderates the nucleation rate by gradually releasing Cu^{2+} into the system. This slow and directional ion supply promotes anisotropic crystal growth, where new material preferentially deposits at high-energy tips, resulting in branched dendrite formation. Furthermore, the crystal habit of Cu_2S favours growth along specific crystallographic directions due to its inherent lattice anisotropy, reinforcing the formation of tree-like structures rather than isotropic morphologies like nanocubes or nanospheres. In contrast, thermodynamically controlled growth which generally yields nanorods or cubes is avoided here due to the absence of strong facet-capping agents and the dominance of kinetic parameters. Therefore, the dendritic morphology is a result of the synergistic effect of moderate supersaturation, EDA-mediated complexation, and anisotropic lattice growth, all of which are uniquely favoured under the selected reaction conditions.[1]

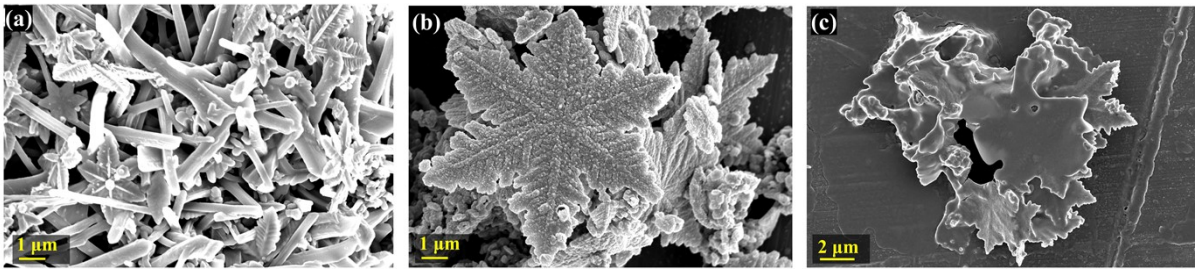

Fig. S1: SEM images of hy-1TMoS2@Cu2S at different temperature (a) 60°C, (b) 80°C and, (c) 100 °C

The HRTEM images for both hy-2H MoS2 and hy-1T MoS2 are given below. In the figure it represents the HRTEM images along with the FFT in the inset. From the calculation, the lattice fringe distance for hy-2H MoS2 is ~0.597 nm (5.97 Å) and for hy-1T MoS2 is ~0.805 nm (8.05 Å). These values are meticulously aligned with the characteristic (002) peak of MoS2. Also, the calculated d spacing values from XRD analysis i.e. 6.16 Å and 8.54 Å, for hy-2H MoS2 and hy-1T MoS2, respectively, match with lattice fringes distance got from

HRTEM. Hence, successful synthesis of both hy-2H MoS_2 and hy-1T MoS_2 can be said to be confirmed.

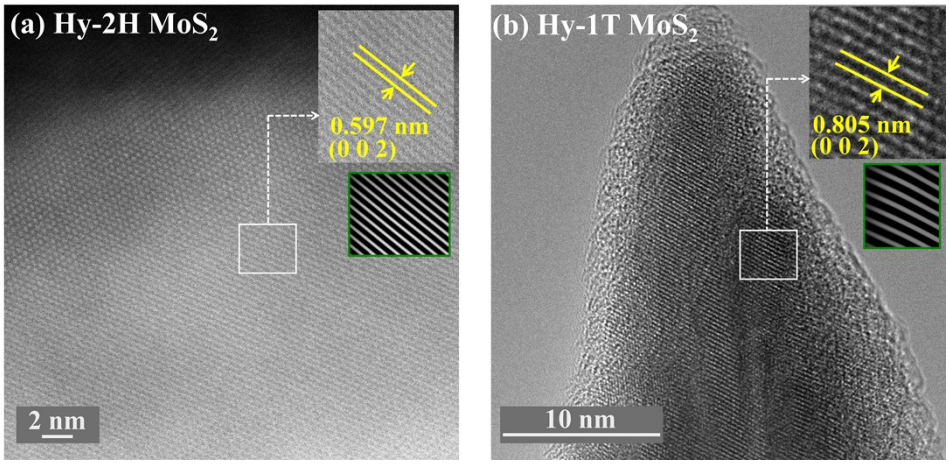

Fig. S2: HRTEM images along with the FFT in the inset (a) Hy-2H MoS_2 and (b) Hy-1T MoS_2

XRD analysis

The average interlayer distance (d) is calculated from Bragg's equation (eq. 1). The crystallite size is calculated from Scherrer's formula (eq. 2). Micro strain(ε) and dislocation density (δ) were calculated using the equations (3,4)

$$n\lambda = 2d\sin\theta \qquad S1$$

$$D = \frac{K\lambda}{\beta\cos\theta} \qquad S2$$

$$\varepsilon = \frac{\beta}{4\tan\theta} \qquad S3$$

$$\delta = \frac{1}{D^2} \qquad S4$$

n is a positive integer, λ is the wavelength of the X-ray (0.154 nm), θ is the diffraction angle. D is the crystallite size, K is the Scherrer constant 0.9, λ is the wavelength (0.154 nm), β is the full width of half maxima. All the values are tabulated in Table S1.

Table S1: Analysis of XRD parameters

Composite	d (Å)	D (nm)	$\delta \times 10^{-3}$ (lines/nm^2)	$\varepsilon \times 10^{-3}$
Hy-2H MoS_2	6.16	3.83	187.91	53.57
Hy-1T MoS_2	8.54	3.18	159.72	83.27
Hy-1T MoS_2@Cu_2S	11.13	21.43	32.89	16.56

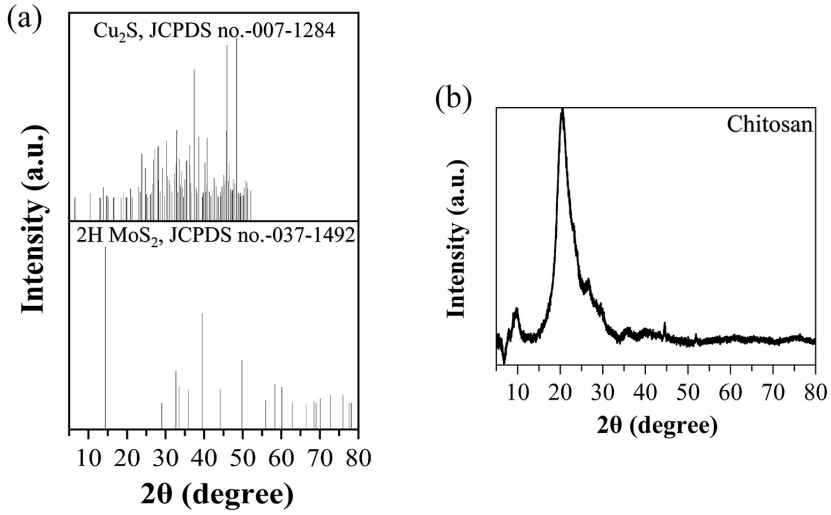

Fig. S3: (a) Standard JCPDS pattern of Cu_2S and 2H MoS_2, (b) XRD pattern chitosan

FT-IR and BET study

As shown in figure S3a in SI, a broad absorption band near ~3400 cm^{-1} corresponds to the O–H stretching vibrations of water molecules adsorbed on the metal surface. Additionally, small peaks observed in the range of ~1620–1560 cm^{-1} can be attributed to the presence of amide bonds, likely originating from residual chitosan or thiourea in the reaction mixture.[2] The peak near ~1400 cm^{-1} is associated with the S=O stretching vibration, which may result from aerial oxidation of the sample. Furthermore, the stretching vibration of the C=S bond is evidenced by a small peak in the ~800–900 cm^{-1} region, consistently observed across all samples except for bulk-2H MoS_2. Notably, a peak at ~480 cm^{-1} corresponds to the Mo–S

stretching vibration in MoS_2,[3] confirming its structural integrity. In the case of the hy-1T MoS_2@Cu_2S composite, the characteristic Cu–S vibrational stretching is identified at ~612 cm^{-1}, further supporting the successful incorporation of Cu_2S into the composite matrix.[3]

To evaluate the accessible surface area and pore size distribution, BET analysis was performed on both the synthesized MoS_2 samples and the composite, as these parameters are crucial in determining the electrochemical efficiency of electrode materials. The nitrogen adsorption-desorption isotherm demonstrated characteristics of a type IV profile, indicative of mesoporous structures. However, minor deviations from the conventional type IV behaviour were observed, likely arising from structural or dynamic modifications occurring within the pores during adsorption and desorption. The isotherm exhibited a capillary condensation step accompanied by an H_3-type hysteresis loop, further corroborating the presence of mesopores (Figure S3b). From the BJH pore size distribution curve (Figure S3c) it is evident an average pore diameter of all the synthesized materials lies between 16-28 nm (well below 50 nm), which clearly classifies it as mesoporous, as per IUPAC guidelines. The measured surface area and total pore volume of hy-1T MoS_2@Cu_2S were determined to be 32 $m^2\ g^{-1}$ and 0.09 cc g^{-1}, respectively, surpassing the values obtained for all MoS_2 samples under investigation (refer to Table S2 in SI). The increased surface area significantly improves electrolyte interaction with the electrode material, thereby enhancing charge storage capabilities. Moreover, the mesoporous architecture facilitates efficient electrolyte penetration through the porous network, which in turn promotes ion transport and contributes to a substantial improvement in C_{sp}.

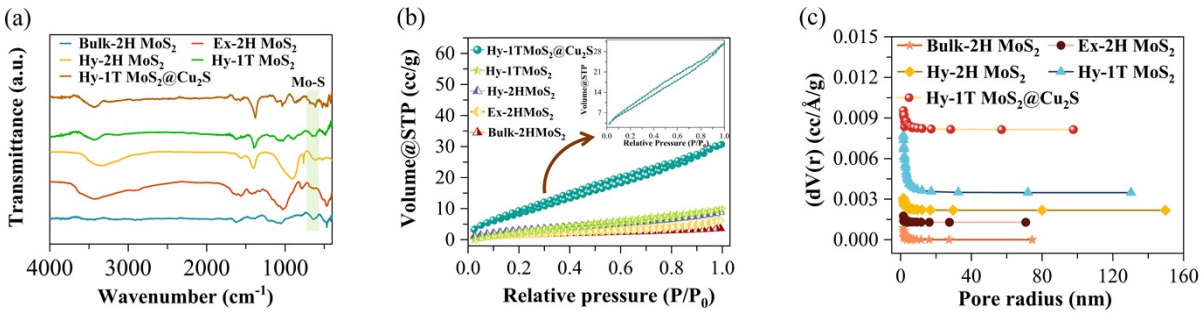

Fig. S4: (a) FT-IR spectra of all the prepared MoS_2 and hy-1T MoS_2@, (b) adsorption-desorption isotherm with the isolated isotherm of the composite in the inset, and (c) BJH pore size distribution of all the synthesized materials

Table S2: BET surface area and pore size measurements of all the prepared materials

Composites	BET surface are (m^2 g^{-1})	Pore diameter (nm)
Bulk-2H MoS_2	13	16.15
Ex-2H MoS_2	14	16.41
Hy-2H MoS_2	16	28.04
Hy-1T MoS_2	22	25.37
Hy-1T MoS_2@Cu_2S	32	22.18

Band-gap energy calculation

Tauc plot equation for direct allowed transition, (equation S2)

$$(\alpha h\lambda)^{1/n} = A(h\lambda - E_g) \qquad S5$$

α is the absorption coefficient, hν is the photon energy, A is a constant, E_g is the band gap energy, and n =0.5 for direct allowed transition

XPS analysis

The figure S3a in SI represents the overall survey scan of the composites in the range of 0-1000 eV. The peaks at 233 eV (Mo 3d) and 160 eV (S 2p) affirm the presence of Mo and S, indicating the successful synthesis of MoS_2 across all samples. Additionally, the Cu 2p peak

~935 eV emerges exclusively in hy-1TMoS_2@Cu_2S confirming the incorporation of Cu_2S into the composite. The other minor peaks at ~530 eV (O 1s) and 283 eV (C 1s) are due to oxygen and carbon surface contaminants, likely due to atmospheric exposure during sample handling. The S 2p spectrum (figure S3b in SI) further supports the formation of metal-sulfide bonds. The peak at ~163 eV deconvolutes into two distinct signals, S $2p_{3/2}$ (~162.4 eV) and S $2p_{1/2}$ (~164 eV), which are characteristic of sulfur in MoS_2.[4] Notably, in hy-1T MoS_2@Cu_2S, the S $2p_{3/2}$ peak experiences a subtle shift, likely due to changes in electron density distribution caused by Cu_2S incorporation. This electron redistribution alters the local chemical environment of sulfur atoms, thereby slightly modifying their binding energy. Such shifts often indicate strong electronic coupling between Cu_2S and MoS_2, which may enhance charge transfer properties in the composite. The Cu 2p spectrum of hy-1T MoS_2@Cu_2S (Figure S3c in SI) presents two well-defined peaks at ~930.1 eV and ~950.1 eV, corresponding to Cu $2p_{3/2}$ and Cu $2p_{1/2,}$ respectively. The observed spin-orbit splitting of ~20 eV is consistent with Cu(I) oxidation state, confirming the formation of Cu_2S.[5] The presence of Cu(I) further reinforces the chemical stability of the composite and suggests a synergistic interaction between Cu_2S and MoS_2, which play a crucial role in enhancing electrochemical performance. All the binding energies have been listed below in table S3 in SI.

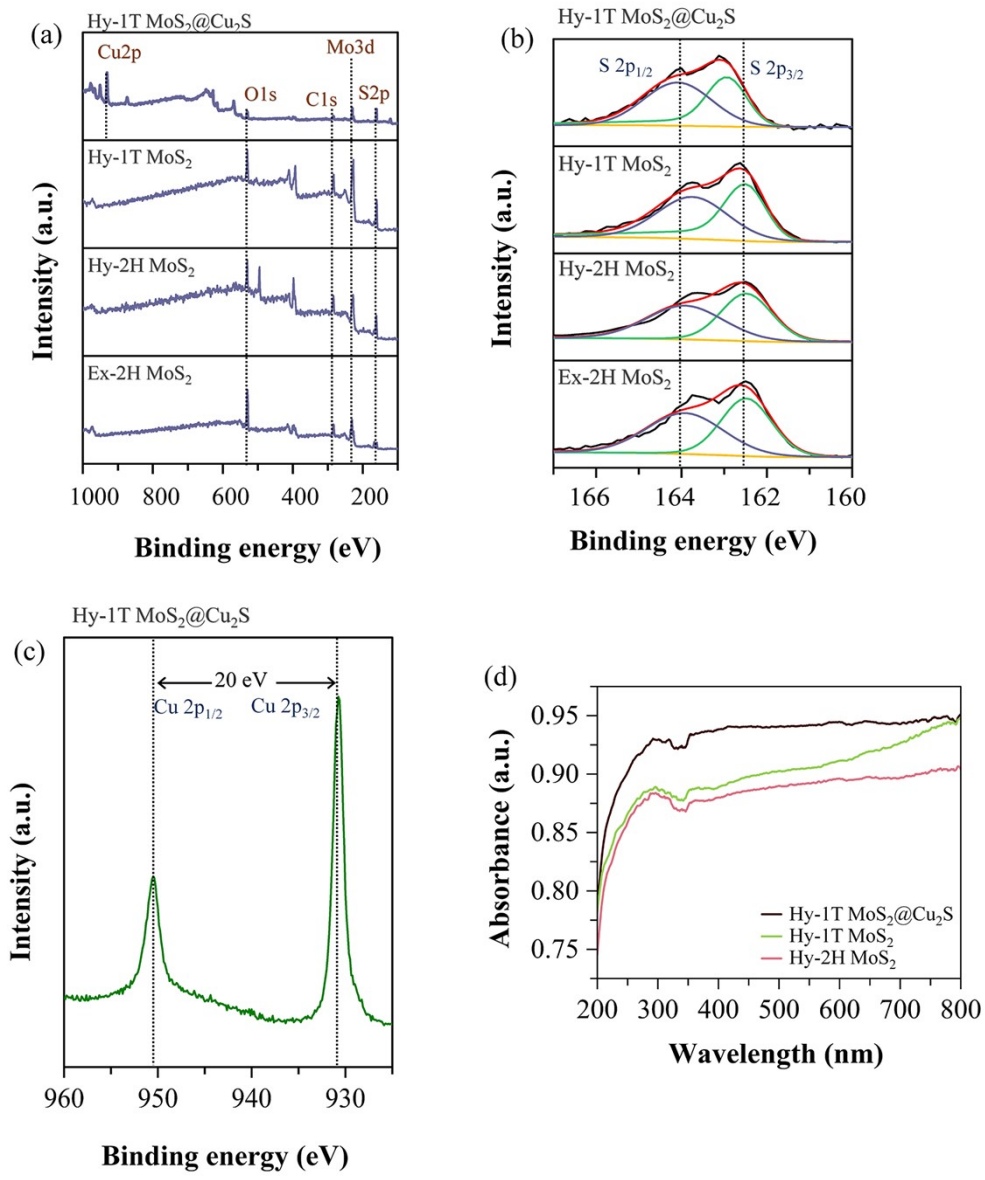

Fig. S5: (a) Survey scan of hy-1T MoS_2@Cu_2S, (b) S 2p spectra of all the prepared MoS_2 and hy-1T MoS_2@Cu_2S, (c) Cu 2p spectra of hy-1T MoS_2@Cu_2S, and (d) UV-Vis spectra of hy-1T MoS_2@Cu_2S, hy-1T MoS_2 and hy-2H MoS_2

Table S3: Peak positions of each element from CCS@CNT-x

Materials	**Cu $2p_{3/2}$ (eV)**		**Cu $2p_{1/2}$ (eV)**	
Hy-1T MoS_2@Cu_2S	930.1 eV		950.1 eV	
Materials	**Mo $3d_{3/2}$ (eV)**		**Mo $3d_{5/2}$ (eV)**	
	2H	**1T**	**2H**	**1T**
Ex-2H MoS_2	233.9	-	230.7	229.1
Hy-2H MoS_2	233.7	-	230.5	228.9
Hy-1T MoS_2	234	233	230.6	229.7
Hy-1T MoS_2@Cu_2S	233.9	232.8	230.5	229.6
Composite	**S $2p_{3/2}$ (eV)**		**S $2p_{1/2}$ (eV)**	
Ex-2H MoS_2	162.9		164	
Hy-2H MoS_2	162.5		164	
Hy-1T MoS_2	162.4		163.7	
Hy-1T MoS_2@Cu_2S	162.4		164.1	

Electrochemical characterization

The electrochemical measurements such as cyclic voltammetry (CV), chronopotetiometry i.e. galvanostatic charge-discharge (GCD), electrochemical impedance spectroscopy (EIS) and linear sweep voltammetry (LSV) were measured using CHI760E electrochemical instrument.

Electrode fabrication for supercapacitor application

The working electrode was prepared by mixing active materials with carbon black as conductive support and PVDF as binder in a ratio of 8:1:1 (w/w/w) in the presence of NMP solvent to form a slurry. The prepared homogeneous paste was then slowly casted on 1.5 × 1.5 cm^2 stainless steel (SS) sheet (thickness 0.116 mm) and dried completely in open air for 24 h. The mass loading of hy-1T MoS_2@Cu_2S was ~ 12 mg. SS was cleaned thoroughly

using ultrasonication prior to use as a current collector. A three-electrode set-up was formed using Pt and Ag/AgCl electrode as counter and reference electrode, respectively and 2 M KOH as the supporting electrolyte for the investigation of the electrode performance.

The specific capacitance and areal capacitance of all the CCS@CNT-x composites was calculated using equation S6a and S6b respectively

$$C_{sp} = \frac{i}{m} \times \frac{\Delta t}{\Delta V} \quad \text{S6a}$$

$$C_{sp(areal)} = \frac{i}{A} \times \frac{\Delta t}{\Delta V} \quad \text{S6b}$$

where, C_{sp} is specific capacitance in F g^{-1}, *i/m* is the applied current density in A g^{-1}, Δt is the discharge time in s, ΔV is the voltage window in V, $C_{sp(areal)}$ is the areal capacitance in mF cm^{-2}, i is the input current in A, A is the area of the current collector in cm^2.

For the device, a two-electrode set-up was designed. The as-mentioned SS was prepared as working electrode following the same method. hy-1T MoS_2@Cu_2S was used as anode material and MnO_2 as cathode, coated over SS and separated by PVA-KOH gel.

Precise mass loading of the electrode material is calculated using the charge-balance equation (equation S7) as given below:

$$\frac{m^+}{m^-} = \frac{C^- V^-}{C^+ V^+} \quad \text{S7}$$

m is mass of the active electrode materials, C is the specific capacitance and V is the voltage window, the superscripts + and – denotes positive and negative, respectively. Using this equation, active mass used for the device is 4 mg of hy-1TMoS_2@Cu_2S and ~18 mg of MnO_2.

Henceforth, the entire electrochemical measurements, i.e., CV, GCD and EIS were conducted. To effectively manage a supercapacitor's storage capacity and ensure swift energy release, it is crucial to evaluate the energy density (E) and power density (P) of the device. Those are calculated as per the equations given below (equation S8 and S9)

$$E = \frac{1}{2} \times \frac{C \times V^2}{3.6} \quad \text{S8}$$

$$P = \frac{E \times 3600}{t} \quad \text{S9}$$

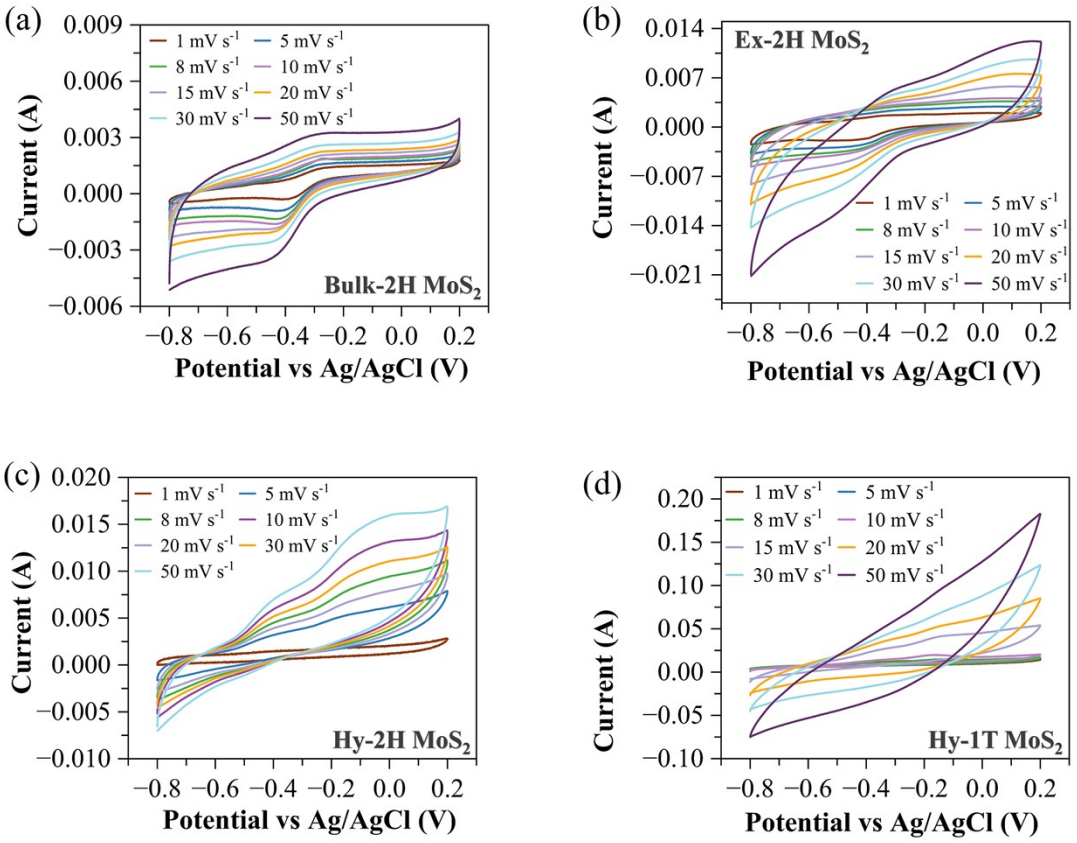

Fig. S6: CV diagram of (a) Bulk-2H MoS_2, (b) Ex-2H MoS_2, (c) Hy-2H MoS_2, and (d) Hy-1T MoS_2.

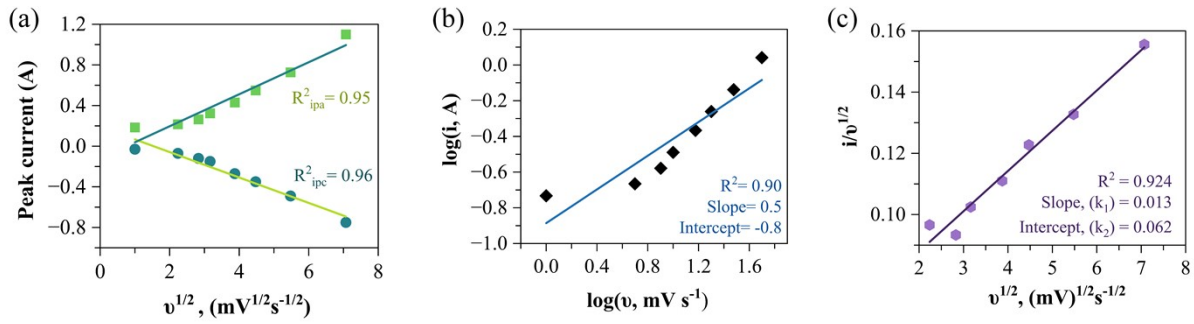

Fig. S7: Electrochemical characterization of hy-1T MoS_2@Cu_2S (a) electrokinetic study, (b) calculation of b value, and (c) calculation of k_1 and k_2.

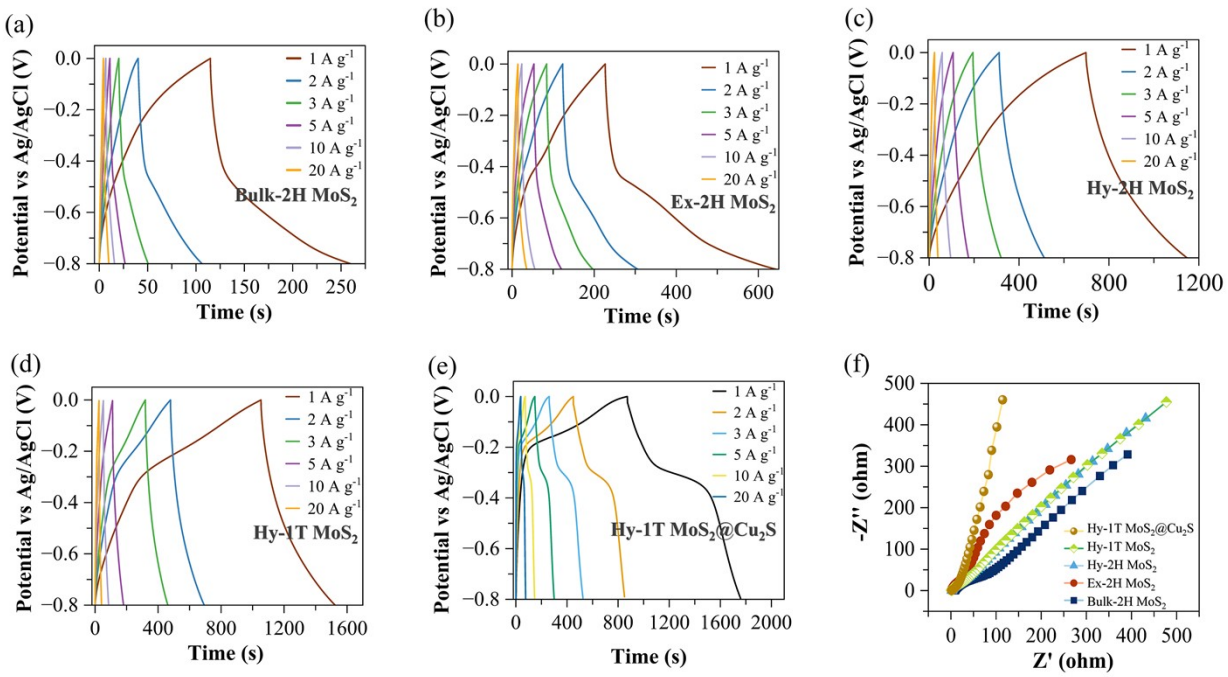

Fig. S8. Comparison among GCD curves of (a) bulk-2H MoS_2, (b) ex-2H MoS_2, (c) hy-2H MoS_2, (d) hy-1T MoS_2, (e) hy-1T MoS_2@Cu_2S at 1 A g^{-1} and (f) Nyquist plot.

Table S4a: C_{sp} values of CCS@CNT-x in varying current densities

Current Density A g^{-1} / Materials	1	2	3	5	10	20
Bulk-2H MoS_2	178	160	112	100	75	72
Ex-2H MoS_2	520	460	423	406	312	302
Hy-2H MoS_2	558	505	480	425	350	325
Hy-1T MoS_2	585	515	506	437	375	355
Hy-1T MoS_2@Cu_2S	1118	1017	986	906	875	850

Table S4b: Areal capacitance values in mF cm^{-2} of CCS@CNT-x in varying current densities

Current Density A g^{-1} / Materials	1	2	3	5	10	20
Bulk-2H MoS_2	79	71	50	45	33	31
Ex-2H MoS_2	231	204	188	180	138	130
Hy-2H MoS_2	248	224	213	188	155	143
Hy-1T MoS_2	260	228	225	194	166	157
Hy-1T MoS_2@Cu_2S	497	452	438	402	388	377

Table S5: Values of solution resistance and charge transfer resistance of CCS@CNT-x

Composites	**R_s (Ω)**	**R_{ct} (Ω)**
Bulk-2H MoS_2	9.10	49.13
Ex-2H MoS_2	2.18	26.04
Hy-2H MoS_2	2.16	17.10
Hy-1T MoS_2	1.24	15.21
Hy-1T MoS_2@Cu_2S	1.16	8.29

Table S6: A comparison table of electrochemical performance

Composite System	C_{sp} (F g^{-1}) at 1 A g^{-1}	Voltage Window (V)	Morphology	Energy Storage Mechanism	Key Highlights	Ref
Hy-1T MoS_2@Cu_2S	1118	1.0	Snowflake-like nanosheets	Pseudo-capacitive (battery-type) + fast ion transport	Cu_2S stabilizes 1T phase of MoS_2, prevents restacking, enhances conductivity; high-performance from synergistic nanostructure.	*This work*
TiS_2/MoS_2	701	0.7	Hierarchical microflower morphology	Pseudo-capacitive	Combination of microspheres and nanosheets increases active surface area but lacks phase stabilization or conductivity control.	6
SnO_2–MoS_2	458	0.6	SnO_2 nanoparticle on the surface of MoS_2 sphere	Pseudo-capacitive (battery-type)	SnO_2 enhances surface interaction but limited by voltage range and lacks phase-engineered MoS_2 or high active exposure.	7
MoS_2/ Graphene (9:1)	295	1.0	Thin flakes uniformly on graphene	EDLC + limited pseudocapacitance	Graphene boosts conductivity; overall performance is modest due to weak redox contribution from MoS_2.	8
Mo_2C@ MoS_2	-	-	MoS_2 nanosheet grown on Mo_2C flakes	Pseudo-capacitive inter-calation	Mo_2C acts as conductive scaffold and current collector; strong Mo_2C-MoS_2 interface enables fast Na^+ intercalation	9

Petal-like 1T-MoS_2	466	0.3	Nanoscale petals	Pseudo-capacitive	Porous and thin layers improve ion transport but lacks heterojunction design and stability control, and hence very poor voltage window	10
Cu_2S/ MoS_2@CM @rGO	931	0.5	nanosphere	Pseudo-capacitive	Prevents MoS_2 restacking and enhances redox kinetics, but lacks phase control and shows less morphological complexity	3
ethylene glycol intercalated Co doped MoS_2	1056	1.0	nanoflakes	Surface controlled pseudo-capacitive	Hierarchical confinement activates edge and basal sites MoS_2 for fast pseudocapacitive K^+ storage, but lacks hybrid-phase synergy.	11

Comparative study between hy-2H MoS_2@Cu_2S and hy-1T MoS_2@Cu_2S

The hy-2H MoS_2 was also used as template for fabricating the composite electrode following the same synthesis route in order to provide a comparative understanding of phase-dependent performance. The formation of hy-2H MoS_2@Cu_2S is confirmed by the XRD spectra given in Figure S9a, where the characteristic (002) peak of 2H phase is present at $2\theta \approx 14.2°$. Afterwards, SEM analysis of this composite confirmed the emergence of a dendritic, snowflake-like morphology. However, the structural features, such as branching density (the length of dendritic petal is ~0.75-1.5 μm), symmetry, and definition, were notably less pronounced compared to the 1T- MoS_2@Cu_2S system (figure S9 b and c). This indicates that while Cu2S was able to nucleate and grow on the 2H-MoS_2 surface, the degree of structural anisotropy and interfacial interaction was weaker than in the 1T-based system. This is likely

due to the limited conductivity and lower surface reactivity of 2H- MoS_2, which may hinder effective nucleation and oriented growth of the Cu_2S branches.

Electrochemical characterizations further validated these morphological observations. The CV curves (Figure S9 d) clearly showed a smaller enclosed area for the 2H-MoS_2@Cu_2S electrode compared to the 1T-based composite, indicating a reduced charge storage capability. Furthermore, GCD analysis revealed a significant voltage drop at the beginning of the discharge curve for the 2H-MoS_2@Cu_2S composite (Figure S9 e), which is indicative of higher internal resistance and poor electrochemical reversibility. This large iR drop not only compromises the energy efficiency of the electrode but also directly impacts the calculated C_{sp}, which was found to be 542 F g^{-1} at 1 A g^{-1}, substantially lower than that of the 1T-MoS_2@Cu_2S composite (1118 F g^{-1}). These findings further underscore the advantage of using the metallic 1T phase of MoS_2, which not only supports the formation of a more defined dendritic architecture but also facilitates improved charge transport and electrochemical activity in the composite electrode.

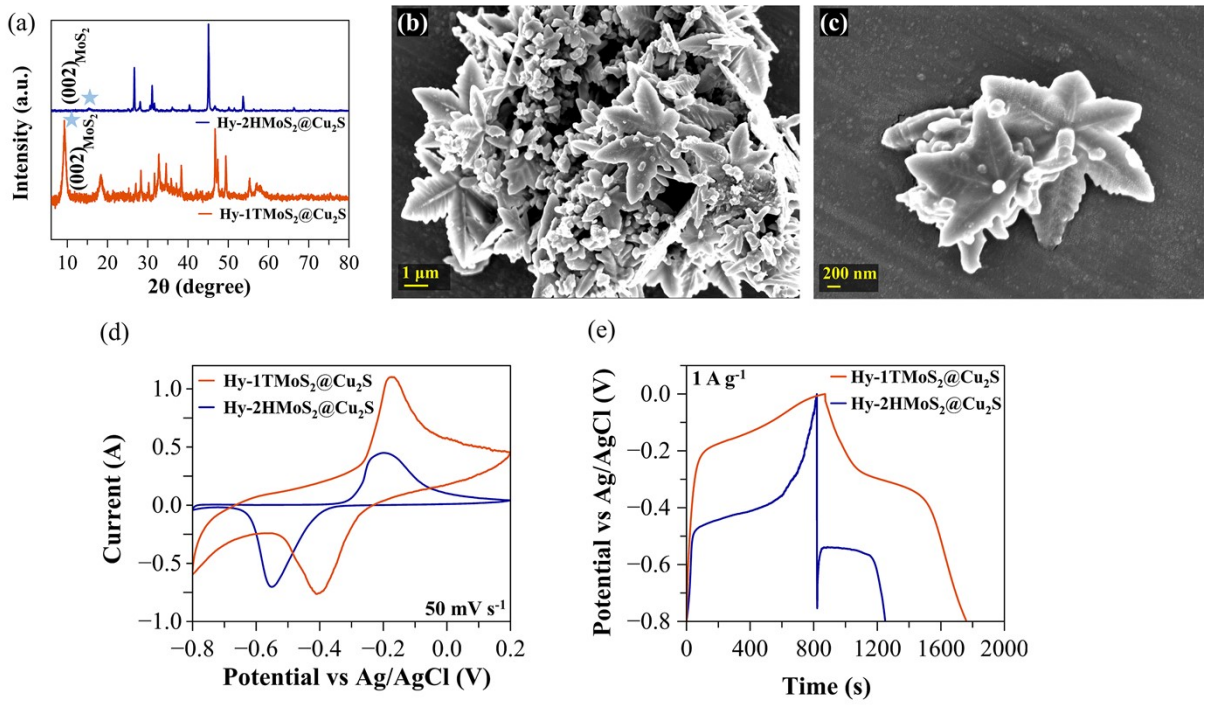

Fig. S9. Comparative study of hy-2HMoS_2@Cu_2S and hy-1TMoS_2@Cu_2S: (a) XRD spectra showing the presence of characteristic (002) peak of MoS_2, (b) and (c) SEM images at different magnification, (d) CV curve of both the composite, and (d) GCD curve of both the composite.

Preparation of MnO_2

MnO_2 was also synthesized by a hydrothermal method. $KMnO_4$ and $MnCl_2.4H_2O$ were mixed together in water in 2:3 M ratio. After stirring for 30 min the solution was filled in a 50 mL Teflon-lined stainless-steel autoclave and kept in the furnace at 180 °C for 24 h. After cooling at room temperature, it was washed completely with DI water and ethanol.

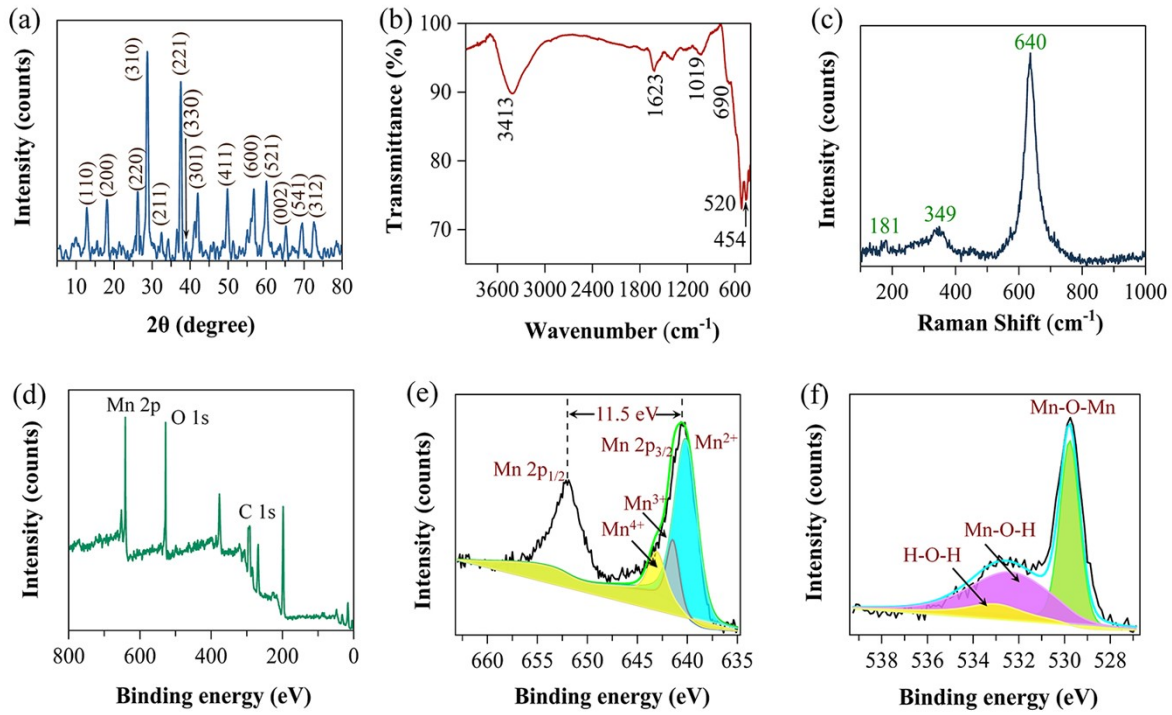

Fig. S10: Characterization of MnO_2 (a) XRD spectra, (b) FT-IR spectra, (c) Raman spectra, (d) XPS overall spectra, (e) Mn 2p spectra and (f) O 1s spectra.

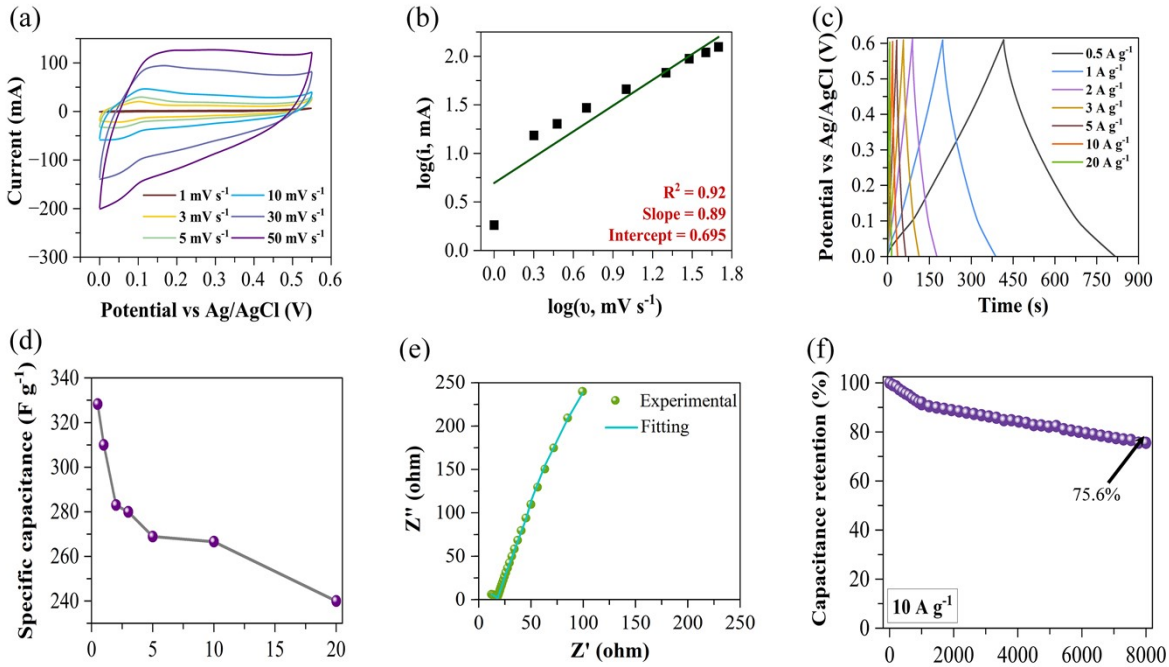

Fig. S11: Electrochemical characterization of MnO_2 (a) CV diagram, (b) calculation b value, (c) GCD curve, (d) C_{sp} values at different current densities, (e) EIS spectra and (f) cycle stability.

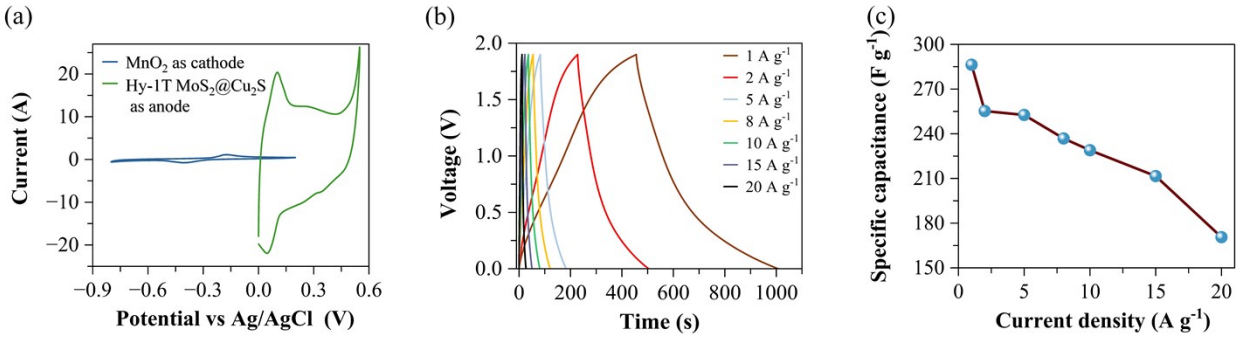

Fig. S12: (a) voltage window comparison of the cathode and anode at 10 mV s^{-1}, (b) GCD curves of the device at different current densities, and (c) Study of specific capacitance of the device with respect to varying current density.

Stress stability test of hy-1T MoS_2@Cu_2S//MnO_2

To evaluate practical feasibility, electrochemical performance of our hy-1T MoS_2@Cu_2S//MnO_2 composite device have been performed under various stress conditions:

1. Mechanical Bending Test: We tested the device under a 45° bending angle and recorded the CV curves. The results revealed negligible change in performance, confirming the mechanical robustness of the composite structure under deformation (figure S13a).
2. High-Rate Long-Term Cycling Test at Low Mass Loading: A low mass loading device was cycled at 20 A g^{-1} for 15,000 cycles, showing excellent retention (~95%) with minimal performance decay, indicating long-term electrochemical stability.
3. High Mass Loading Test: A device fabricated with high mass loading (~12 mg composite and ~50 mg MnO_2) was cycled at a high current density of 40 A g^{-1} for 8000 cycles. It shows a slight decrease (~70% retention) than the low mass loading cycling test (figure S13b). This reduction in retention is primarily due to well-known limitations associated with thick electrodes, such as sluggish ion diffusion, lower active material utilization, and increased internal resistance.[17] These factors often lead to a drop in performance at high mass loadings. Nonetheless, achieving 70% retention after 8000 cycles under such demanding conditions still reflects the good mechanical and electrochemical stability of our hy-1T MoS_2@Cu_2S//MnO2 system. This performance affirms the structural integrity and long-term durability of the composite. Thus, it shows a promising real-world energy storage application that demand higher material loading.

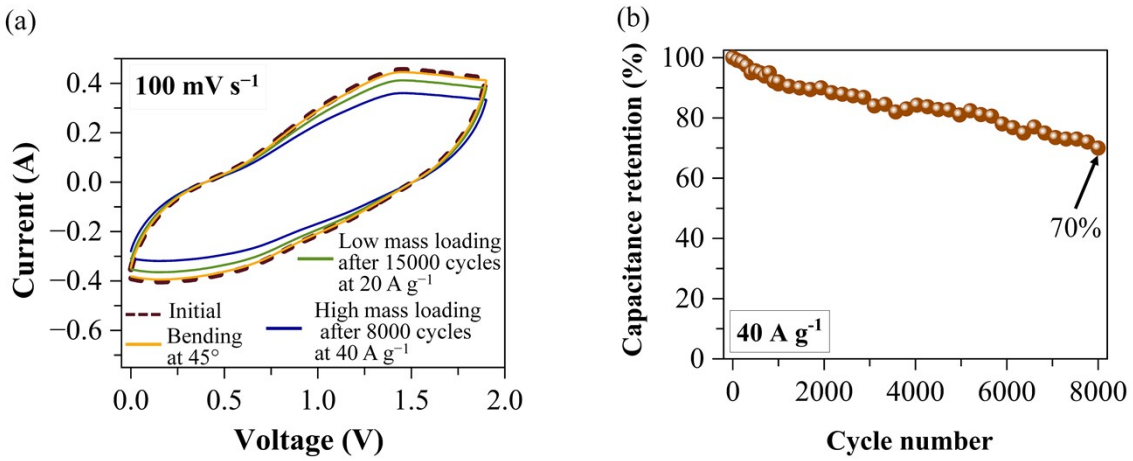

Fig. S13. (a) CV curves after several stress-stability tests and (b) cyclic stability of the device at high mass loading.

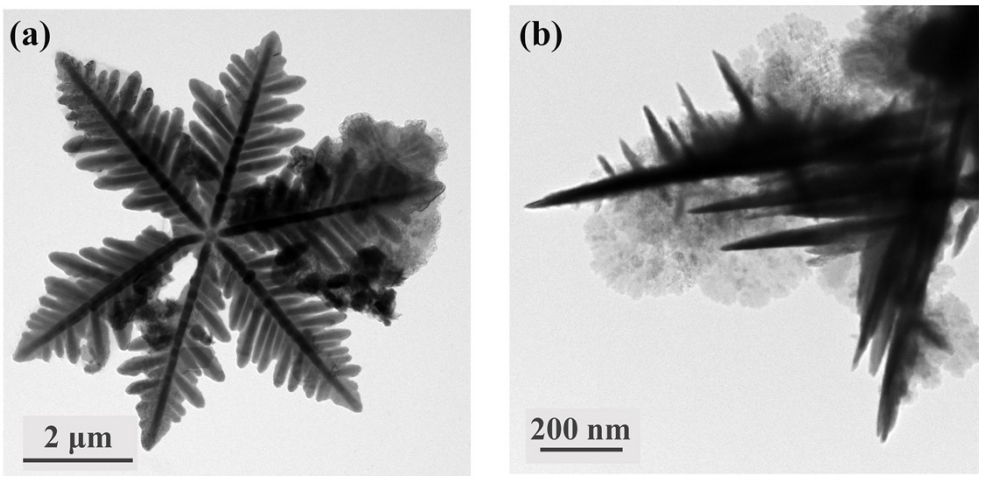

Fig. S14: TEM images after cyclic stability test (a) at 2 µm and (b) at 200 nm.

Reference

1. A. Arneodo, F. Argoul, J. F. Muzy and M. Tabard, *Physica A: Statistical Mechanics and its Applications*, 1992, **188**, 217–242.
2. C. Lustriane, F. Dwivany, V. Suendo and M. Reza, *Journal of Plant Biotechnology*, 2018, **45**, 36–44.
3. H. Xu, Y. Zhang, F. Liu, Z. Yang, J. Xu and J. Liu, *ACS Appl. Nano Mater.*, 2024, **7**, 21340–21350.
4. H. Zhang, L. Deng, J. Chen, Y. Zhang, M. Liu, Y. Han, Y. Chen, H. Zeng and Z. Shi, *Chemical Engineering Journal*, 2022, **446**, 137364.
5. M. Kumar, V. Bhatt, O. S. Nayal, S. Sharma, V. Kumar, M. S. Thakur, N. Kumar, R. Bal, B. Singh and U. Sharma, *Catal. Sci. Technol.*, 2017, **7**, 2857–2864.
6. G. Nabi, W. Ali, M. Tanveer, T. Iqbal, M. Rizwan and S. Hussain, *Journal of Energy Storage*, 2023, **58**, 106316.
7. K. Rafique, N. Hassan, M. Z. U. Shah, S. I. Al-Saeedi, A. Shah, M. S. U. Shah, U. Aziz, M. Sajjad, A. A. Alanazi and H. M. A. Hassan, *Surfaces and Interfaces*, 2024, **44**, 103650.
8. C. S. Bongu, M. R. Krishnan, A. Soliman, M. Arsalan and E. H. Alsharaeh, *ACS Omega*, 2023, **8**, 36789–36800.
9. Z. Khanam, L. Luo, M. Mushtaq, J. Li, H. Yang, T. Ouyang, M.-S. Balogun and A. Pan, *Nano Energy*, 2024, **125**, 109590.
10. M. Mohan, N. P. Shetti and T. M. Aminabhavi, *Journal of Energy Storage*, 2023, **58**, 106321.
11. L. Kang, S. Liu, Q. Zhang, J. Zou, J. Ai, D. Qiao, W. Zhong, Y. Liu, S. C. Jun, Y. Yamauchi and J. Zhang, *ACS Nano*, 2024, **18**, 2149–2161.
12. H. Li, H. Li, Z. Wu, L. Zhu, C. Li, S. Lin, X. Zhu and Y. Sun, *Journal of Materials Science & Technology*, 2022, **123**, 34–40.

13. R. Thangappan, S. Kalaiselvam, A. Elayaperumal, R. Jayavel, M. Arivanandhan, R. Karthikeyan and Y. Hayakawa, *Dalton Trans.*, 2016, **45**, 2637–2646.

14. H. Li, Z. Wei, X. Yuan, Y. Zhao, Q. Jia, Y. Li, D. Ma, B. Li, Y. Zhang and X. Zhu, *Journal of Power Sources*, 2024, **608**, 234648.

15. S. Irfan, M. Aalim, M. H. Flaifel, I. Nazir, M. A. Shah, M. Q. Lone, A. Firdous, A. H. Pandith and G. N. Dar, *Journal of Energy Storage*, 2025, **106**, 114788.

16. X. Wu, X. Yu, Z. Tian, H. Li and J. Xu, *ACS Nano*, 2025, **19**, 9292–9303.

17. C. Mevada and M. Mukhopadhyay, *Ind. Eng. Chem. Res.*, 2021, **60**, 1096–1111.